Quality control tool of electrode coating for lithium-ion batteries based on X-ray radiography

Aurélien Etiemble, N. Besnard, J. Adrien, P. Tran-Van, L. Gautier, B. Lestriez, E Maire

Quality control tool of electrode coating for lithium-ion batteries based on X-ray radiography

A. Etiemble[1], N. Besnard[2,3], J. Adrien[1], P. Tran-Van[3], L. Gautier[4], B. Lestriez[2], E. Maire[1,*]

(1) Institut national des sciences appliquées de Lyon, Laboratoire MATEIS, CNRS UMR5510, F-69621 Villeurbanne, France.

(2) Institut des Matériaux Jean Rouxel (IMN), CNRS UMR 6502, Université de Nantes, 44322, Nantes Cedex 3, France

(3) Renault technocentre, 78084 Guyancourt, France

(4) Umicore Rechargeable Battery Materials, 1000 Brussels, Belgium

Corresponding authors at:

* INSA-Lyon MATEIS CNRS UMR5510, F-69621 Villeurbanne, France
Tel.: +33 4 72 43 88 61; fax: +33 4 72 73 85 39.
E-mail addresses: eric.maire@insa-lyon.fr

Abstract

A simple and efficient method, based on X-ray radiography, is developed to check the quality (homogeneity of the thickness, presence of defects) of NMC-, LFP- and NMC/LFP-based electrode coating for Li-ion batteries at the scale of several cm^2 with a resolution of 20µm. As a first step, the attenuation coefficient of NMC- and LFP-based coating is experimentally determined according to the Beer-Lambert law. Then, the attenuation coefficient of each active material is estimated from these experimental results and X-ray attenuation databases, which allows establishing an attenuation law for any coating composition. Finally, thanks to this relationship, the thickness can be evaluated in each spot of the film and the defects, such as pinholes or broad edges with gradual decrease of the thickness coating, can be detected. The analysis of NMC-, LFP- and NMC/LFP-based electrodes shows that the coating quality decreases as coating thickness increases and as the nanometric *vs.* micrometric material content increases in the coating composition. This reveals detrimental aspects of nanomaterials with respect to their use in composite electrode manufactured through conventional slot-die or casting process.

Keywords*: lithium ion battery; electrode; processing; X-ray radiography*

1. Introduction

Lithium-ion batteries are manufactured by assembling three foils: the negative electrode, the positive electrode and the separators **[1-4]**. After blending of active materials, additive, binder and electrolyte, the electrodes are made by a coating process of the active layer on a copper (anode) or aluminum (cathode) substrate. After drying, the coating is then compressed (calendered) to optimize the porosity. Electrodes and separators are cut and, finally, the cells are stacked. In this process, the coating and the compression plays a major role on the battery performances **[2]**. The initial capacity of the battery but also the cycle life is strongly influenced by the processing and electrode fabrication **[2, 4]**. In addition, simulations of the impact of variations in electrode manufacturing on Li-ion batteries show that the electrode thickness and density are the most significant parameters to optimize the useful capacity of battery module **[4]**.

The electrodes have to be continuous, homogeneous and smooth (i.e. a low thickness deviation). The coating method and the slurry properties are the main factors playing a role on process efficiency **[3]**. Also, appropriate slurry rheological characteristics, density, porosity, viscosity, adhesion have to be optimized **[5-8].** The coating process must result in layers with very homogeneous thickness and density distribution as many heterogeneities in the layer might result in undesired local aging of the electrode **[9]** or poorer rate performance **[10]**.

In this framework, an efficient monitoring of the electrode parameters is required in order to evaluate the process and to detect possible defects in the early stage of the production. In addition, a detection of the electrode coating edges on both sides is required in order to optimally adjust the laser cut during the electrode tailoring **[3]**. An efficient method needs a resolution of a few micrometers to assure complete defect detection and a large visual field to match up the industrial scale. Optical microscopy, beta transmission, infrared radiation and laser caliper are currently applied during industrial electrode manufacturing **[1,**

2, 11, 12]. Thickness heterogeneity, pinholes, divots and agglomerates in the electrodes however are not easily identified during the coating process **[12]**. In addition, beta transmission measurement is an expensive and environmentally hazardous (due to ionizing radiation) technique **[12]**. It requires radioactive sources, which necessitates specialized shielding, services and high levels of security. Raman microscopy has also been previously evaluated as a possible inline characterization technique of battery electrodes **[13]**, but there is however still a need for conventional, efficient and low cost inspection tools in Li-ion batteries quality control.

Radioscopic inspection is one of the most non-destructive testing used for inline monitoring of industrial process, such as lightweight material production, electronic component soldering or food production **[14]**. The use of X-ray radiography also requires ionizing radiation protection but much less restrictive than beta transmission and doesn't induce expensive cost associated with storage and transportation of radioactive sources. X-ray radiography allows visualizing a three-dimensional body, the attenuation of which is projected in a two-dimensional plane. As such, it provides a precise information and localization of structural heterogeneities and defects.

$Li_1Ni_{1/3}Co_{1/3}Mn_{1/3}O_2$ (NMC), compound is a high-capacity electrode material for lithium ion battery which exhibits great structural stability, a higher capacity a lower cost and a better thermal stability than the traditional $LiCoO_2$ cathode. Its high bulk conductivity allows using it as micrometric particles or even clusters of micrometric particles in composite electrodes **[15]**. Such large particles allow higher solid content in the composite electrode layer facilitating a higher energy density, which makes this compound an active material of choice for electric and hybrid electric vehicles **[16]**. $LiFePO_4$ (LFP) compound possesses a better thermal stability than NMC. As a consequence of low bulk conductivity, it can only be used as nanometric particles or as clusters of nanometric particles if these ones are coated by a

thin layer of conducting carbon **[17]**. Additionally, LFP operates at a low voltage, which makes it less attractive for electric and hybrid electric vehicles. Blending different active materials is an approach followed by several automotive battery suppliers intended to optimize the performance of the battery with respect to the automotive operating requirements. By blending two cathode materials the shortcomings of the parent materials can be minimized and the resulting blend can be tailored to have a higher energy or power density coupled with enhanced stability and lower cost **[18]**.

In this paper, a simple and efficient method, based on X-ray radiography, is developed to evaluate the thickness and to detect the defects of positive electrodes based on NMC, LFP, and blends of NMC and LFP for Li-ion batteries.

2. Experimental

2.1. Materials

Several samples with different composition and thickness have been produced for the present study. **Table 1** summarizes composition, thickness (estimated on SEM images) and calculated porosity of the all the studied electrodes. The porosity derives from the electrode weight, thickness and material density. These were prepared with a NMC compound (Cellcore® MX10) and/or a LFP one (PhoLiCat® FE100), both supplied by UMICORE. The NMC is micrometric material in the form of dense spherical clusters whose size ranges from 5 to 17µm (D_{50} = 9.7µm). The LFP is a nanometric material that is more or less agglomerated and the particles/agglomerates size ranges from 0.5 to 10µm. The BET measured specific surfaces are 0.28 and 18-20 $m^2\ g^{-1}$ for NMC and LFP, respectively. Carbon black (Cb) was used as conductive additive, polyvinylidene difluoride (PVdF) as binder and aluminum foil as substrate.

2.2. X-ray Radiography

The X-ray radiography analysis of the electrodes was performed at a pixel size of 20µm using a laboratory tomograph (Phoenix V tome X) described in **[19]**. The X-ray source was operated with a tungsten cathode at a voltage of 80kV and a current of 240µA. Each acquired radiograph consisted in an average of 3 radiographs for each electrode. The electrodes are put orthogonally to the incident beam between the X-ray source and the detector. In this condition, it can be considered that the beam cross the electrode thickness in a straight line.

3. Results and Discussion

3.1. Beer-Lambert Law

X-ray radiography physics is based on the Beer-Lamber law (Eq. 1), which depicts the relationship between the number N of transmitted photons of energy E and the number N_0 of the incident photons of energy E **[20]**.

$$\frac{N}{N_0} = exp\left[-\int_{S\in ray} \mu(S)dS\right] \quad (1)$$

where μ is the attenuation coefficient. In the photoelectric domain, the attenuation coefficient, μ, typically follows the relationship:

$$\mu = K\rho\frac{Z^4}{E^3} \quad (2)$$

where K is a constant, ρ and Z respectively are the density and the atomic number of the investigated material and E is the energy of the incident photon [**20].** For a polychromatic incident beam, like the one emitted by a X Ray tube in a laboratory tomograph, the Beer-Lambert law has to be integrated over the whole photon energy spectrum.

The contrast observed in the X-ray radiograph of a bulky material is explained by this attenuation law because each point of a detector placed behind the sample is situated in front of a different path, each path exhibiting a different value of the integral of μ.

The integral of μ can be approximated by assuming that the X-rays behave like a monochromatic beam exhibiting the average equivalent photon energy of the X-ray tube

spectrum. Strictly speaking, we are aware of the fact that this is slightly wrong especially after crossing the samples as the X-Ray beam is modified (is filtered) differently by every different material. This can however be estimated to be a good first approximation, especially because our samples are rather thin. It will be shown later that this approximation is validated by our different measurements.

Experimentally, all this leads to the relationship (Eq. 3) between the incident intensity I_0 and the outgoing intensity I.

$$I = I_0 e^{-\mu L} \tag{3}$$

where L is the length through the material (the attenuation of the X rays through air before and after the sample is very small and can be neglected) and μ is the attenuation coefficient corresponding to the average equivalent energy.

Figure 1 shows the relative outgoing X-ray intensity histograms in electrode and air areas for various thicknesses of NMC (**Fig. 1A**) and LFP electrodes (**Fig. 1B**). The outgoing intensities are distributed according to a Gaussian function, whose parameters are characteristic of the various paths through the material. This Gaussian distribution has roughly the same spread in the air area for all the samples. The peak center and shape of the Gaussian distribution vary depending on the composition (attenuation coefficient) and the thickness (length through the material) of the electrodes. In order to investigate the thickness heterogeneity, the equivalent average photon energy and the attenuation of the electrode materials must be defined.

3.2. Equivalent photon energy and attenuation coefficients

At this point, the average equivalent energy of the photon X-ray beam emitted by the X-Ray tube is not known. We determine an approximation of this energy in this section using standards with known attenuation but also using our electrodes of known thickness and

porosity composed of unblended materials. We will also use the fact that the carbon component of the electrodes (Cb and PVdF) exhibit negligible attenuation.

The attenuation through titanium and aluminum foils of known measured thickness (14 µm for aluminium and 20 µm for titanium) has firstly been measured using equation (3) and measurements of I and I_0 from radiographs such as those shown in Fig 1. µ was found to be equal to 0.0023µm^{-1} for Ti and 0.00043µm^{-1} for Al.

In the case of electrodes perpendicular to the incident beam, Equation (3) can be expressed as a relationship between the outgoing intensity, I, electrode thickness, T, and porosity, ε:

$$ln\left(\frac{I}{I_{air}}\right) = C - \mu T(1-\varepsilon) \quad (4)$$

where I_{air}, the outgoing intensity in air area and C, a constant associated especially with the attenuation due to the aluminium current collector and the diffraction. The porosity is considered homogeneous inside the electrodes and the outgoing intensities are evaluated as the peak center of the Gaussian distribution (**Fig. 1**).

Figure 2 shows $\ln(I/I_{air})/(1-\varepsilon)$ as a function of the thickness T, estimated on cross-section SEM images, for NMC and LFP electrodes (the blended electrodes were excluded from this analysis). The Beer Lambert law is clearly nicely respected in this figure and a linear evolution is observed for all materials in agreement with equation (4).

The linear fitting parameters are summarized in **Table 2**. The most important information to extract from this table is the value of the slope, µ, that corresponds to the attenuation coefficient of each material for the average equivalent energy of the beam.

Figure 3 shows the attenuation coefficient of NMC, LFP, PVdF, Cb, Al and Ti as a function of the photons energy as tabulated in **[21]**. The attenuation coefficient µ determined previously can be superimposed on these curves as horizontal lines as shown in **Figure 3** and the energy corresponding to the crossing of the µ curves with these particular values of µ can

be extracted from this construction. The figure shows that these energies for all the investigated materials are all very close to 27 ± 2 keV. The equivalent energy of the photon X-Rays can then be assumed to be close to 27 keV. This is in relatively good agreement with what can be expected for the X-Ray tube operated at 80 kV in this study and this validates the concept of average equivalent energy that we used from simplification in the present study.

For any blended NMC/LFP/PVdF/Cb electrodes, the relationship between the outgoing intensity, *I*, electrode thickness (µm), *T*, and porosity, ε, can be established, by taking into consideration these attenuation coefficients, as:

$$\frac{ln\left(\frac{I}{I_{air}}\right)}{(1-\epsilon)} = C - (3.35f_{NMC} + 1.02f_{LFP}) * T * 10^{-3} \quad (5)$$

with *C* sets at -0.02, -0.04 and -0.03, respectively for FLP, NMC and blended LFP/NMC cathodes and, f, the volume density of each highly absorbent material in the composite electrode composition.

The values of *T*, calculated with the equation (5) and averaged over the electrode surface, are shown in **Figure 4** and are in fair agreement with the SEM estimation for all the electrodes.

3.5. Thickness heterogeneity

Thanks to Equation 5 and considering that the phase distribution is homogeneous in the thickness of the electrode, the fluctuation of the intensity in the radiographs can be attributed to thickness fluctuations only and this fluctuation of *T* can thus be mapped for every pixel of the detector, each pixel corresponding to a path through the electrode.

Figure 5 and **Figure 6** show the thickness mapping for NMC, LFP, and blended NMC/LFP electrodes. **Figure 7** shows the width at half maximum of the thickness histograms, which reflects its heterogeneity, as a function of the average thickness. Note that the resulting thickness heterogeneity values are slightly overestimated by this method due to the inherent dispersion of the intensity of the incident beam, as illustrated in **Figure 1** for the

air area (used as reference of the incident beam) and the variability of porosity/density. Also, X-ray tomography investigations show that the surface standard deviation of NMC density is about 3% at this resolution (not shown), namely less than the thickness heterogeneity estimated by X-ray radiography. In addition, the porosity/PVdF/Cb distribution variability should decrease as the LFP content increases due to its nanometric morphology.

For NMC electrodes, the thickness heterogeneity is low and slightly increases as the thickness increases. Also, the thickness appears spatially homogenous in this material (**Fig. 5A and 5B**) with a granular aspect, which could be associated with the clusters/porosity repartition. The heterogeneity of LFP electrodes thickness is much higher than for NMC electrodes and increases more significantly as the thickness increases (**Fig. 5C and 5D**). Large thinner areas are observed on the thickness mapping and could be associated with the coating step during the electrode preparation. The thickness heterogeneity of blended NMC/LFP electrodes also appears high, similar to LFP ones, with exception of the electrode D that has the largest roughness variations of all electrodes (**Fig. 7**). One should note that electrode D has the higher Cb content of all electrodes (**Table 1**).

In manufacturing lithium-ion battery electrodes, the slurry is coated using a slot-die process or cast onto a transfer roll by a doctor blade, which then transfers the slurry to the current collector. The coating quality depends on many parameters, among which the colloidal stability, the rheological properties and the surface tension of the electrode slurry, the roll speed, the gap width between the slot-die or the doctor blade and the current collector **[22]**. The rheological properties of NMP-based electrode slurries containing NMC or LFP active materials, carbon black (Cb) conductive additive, and polyvinylidene difluoride (PVdF) binder have been studied by Bauer *et al*. **[5]**. As a consequence of smaller and nanometric particle size, LFP-based slurries show marked shear thinning behavior (large viscosity variations with shear/flow rate) and stronger elasticity than NMC-based ones. However,

increasing CB and PVdF contents in NMC-based slurries increases their shear thinning behavior and elasticity. These two characters are due in both types of slurries to the establishment of PVdF bridges between LFP and/or CB nanoparticles. Here, the larger roughness variations are observed for slurries that contain these nanoparticles. In particular, high PVdF and Cb contents (electrode D) seem to significantly impact roughness variations. Putting all these results together, it is suggested that marked shear thinning behavior and/or strong elasticity are detrimental properties of electrode slurries with respect to the quality of the resulting coating. An increase of surface roughness with an increase of coating thickness was also measured by Schmitt *et al*. on Graphite/PVdF-based slurries for negative electrodes **[22]**.

3.6. Defects detection

During the slurry coating, pinholes can be left over inside the electrodes due to gas release. This kind of defect, which is detrimental to the calendering step, is not desirable. Some pinholes, characterized by local low attenuation coefficient (i.e. thickness) as shown in **Figure 8A**, can be observed in the thickness mapping of NMC, LFP, and blended NMC/LFP electrodes (**Fig. 5 and 6**). For both NMC and LFP electrodes, they are mostly observed for the highest coating thickness. This is particularly obvious for the LFP electrodes (**Fig. 5D**). The 25/75 blended NMC/LFP electrode, which is the thickest of this group, appears also impacted by this phenomenon. From these results, the thickness seems to be the major parameter, acting negatively on pinhole formation. The difference of maximum thickness between NMC and LFP electrode specimens does not allow investigating precisely the composition influence on this defect appearance. Pinholes could find their origin from air bubbles trapped in the viscous electrode slurries that are more easily removed when the slurry is forced to flow through a narrow gap to form a thin coated layer than through large ones. Shear is also likely to destroy these bubbles and shear is more important for thinner electrodes.

The slurry coating on the copper or aluminum substrate induces broad edges with gradual decrease of the thickness coating. The laser cutting has to be as precise as possible in order to maximize the consistent output electrode surface area. **Figure 8B** shows thickness mapping, from the X-ray radiography, of the coating edge for the thickest (P) NMC electrode. A thickness gradient and a large defect with a trench aspect are observed at the edge of the active layer. This demonstrates the efficiency of the X-ray radiography to evaluate precisely the electrode coating and that this technique allows detecting easily the defects and the edges of the films. In the same way, layer scratch, which can occur during the electrode manufacturing, could be characterized by X-ray radiography as drastic local thickness variation.

4. Conclusion

This study has demonstrated that X-ray radiography, which is a simple and non-destructive analytical technique, is a powerful tool for checking the quality of electrode coating at the scale of several cm^2 with a resolution of 20µm. Radiography is fast so it could also be implemented on much larger surfaces and/or with a different resolution by multiplying the number of fields of view. Methods to evaluate from the acquired radiographs through careful image processing the homogeneity of the electrode thickness and of components distribution, as well as the presence of defects, were described. Care must be taken because of the polychromaticity of the incident beam in a standard laboratory radiographic system. We have tackled this difficulty by assuming and evaluating the average equivalent energy of the beam.

By this X-ray radiography analysis of NMC-, LFP- and NMC/LFP-based electrodes, we quantify the decrease in coating quality with increase in coating thickness and with increase in nanometric vs. micrometric material content in the coating composition. This

reveals detrimental aspects of nanomaterials with respect to their use in composite electrode manufactured through conventional slot-die or casting process.

Manufacturing, well-performing thick electrodes is a critical issue for lithium ion battery application to raise the energy and power densities. Finally, this new analytical technique could be used by industry engineering or researchers to quantify the quality of their coatings at large scale. The setup used here is dedicated to research and does not allow us to achieve roll to roll process control. There would be no difficulties however, to adapt such a device to an in-line control of the fabrication process of such electrodes directly on a fabrication line in the future.

Acknowledgements

The authors would like to acknowledge IMD (Institut de la Mobilité Durable – Sustainable Mobility Institute) for financial support.

References

1. J. Kurfer, M. Westermeier, C. Tammer, G. Reinhart, Production of large-area lithium-ion cells – Preconditioning, cell stacking and quality assurance, CIRP Ann. – Manuf. Technol. 61 (2012) 1-4.
2. G. Lanza, A. Koelmel, S. Peters, A. Sauer, S. Stockey, Automated optical detection of particles and defects on a Li-ion-cell surface using a single-point analysis. IEEE Int. Conf. on Autom. Sci. Eng. (2013).
3. G. Reinhart, T. Zeilinger, J. Kurfer, M. Westermeier, C. Thiemann, M. Glonegger, M. Wunderer, C. Tammer, M. Schweier, M. Heinz, Research and demonstration center for the production of large-area lithium-ion cells, in: G. Schuh, R. Neugebauer, E. Uhlmann (Eds.), Future Trends in Production Engineering, Springer Berlin Heidelberg, 2013, pp. 3-12.
4. B. Kenney, K. Darcovich, D.D. Macneil, I.J. Davidson, Modelling the impact of variations in electrode manufacturing in lithium-ion battery modules, J. Power Sources, 213 (2012) 391-401.
5. W. Bauer, D. Nötzel, Rheological properties and stability of NMP based cathode slurries for lithium ion batteries, Ceram. Int. 40 (2014) 4591-4598.
6. K.Y. Cho, Y. Kwon, J.R. Youn, Y.S. Song, Evaluation of slurry characteristics for rechargeable lithium-ion batteries, Mater. Res. Bull. 48 (2013) 2922-2926.
7. K.M. Kim, W.S. Jeon, I.J. Chung, S.H. Chang, Effect of mixing sequences on the electrode characteristics of lithium-ion rechargeable batteries, J. Power Sources 83 (1999) 108-113.
8. W. Porcher, B. Lestriez, S. Jouanneau, D. Guyomard, Design of aqueous processed thick $LiFePO_4$ composite electrodes for high-energy lithium battery, J. Electrochem. Soc. 156 (2009) A133-A144.

9. T. Takamura, M. Saito, A. Shimokawa, C. Nakahara, K. Sekine, S. Maeno, N. Kibayashi, Charge/discharge efficiency improvement by the incorporation of conductive carbons in the carbon anode of Li-ion batteries, J. Power Sources 90 (2000) 45-51.
10. M. Smith, R.E. Garcia, Q.C. Horn, The effect of microstructure on the galvanostatic discharge of graphite anode electrodes in $LiCoO_2$-based rocking-chair rechargeable batteries, J. Electrochem. Soc. 156 (2009) A896-A904.
11. P. Just, L. Elbert, T. Echelmeyer, M.A. Roscher, Infrared particle detection for battery electrode foils, Infrared Phys. Tech. 61 (2013) 254-258.
12. D. Mohanty, J. Li, R. Born, L.C. Maxey, R.B. Dinwiddie, C. Daniel, I.D.L. Wood, Non-destructive evaluation of slot-die-coated lithium secondary battery electrode by in-line laser caliper and IR thermography methods, Anal. Methods 6 (2014) 674-683.
13. J.-C. Panitz, P. Novák, Raman microscopy as a quality control tool for electrodes of lithium-ion batteries, J. Power Sources 97-98 (2001) 174-180.
14. R. Hanke, T. Fuchs, N. Uhlmann, X-ray based methods for non-destructive testing and material characterization, Nucl. Instr. Methods Phys. Res. 591 (2008) 14-18.
15. K.A. Seid, J.C. Badot, O. Dubrunfaut, M.T. Caldes, N. Stephantm L. Gautier, D. Guyomard, B. Lestriez, Multiscale electronic transport in Li1+xNi1/3-uCo1/3-vMn1/3-wO2: a broadband dielectric study from 40 Hz to 10 GHz, Phys. Chem. Chem. Phys. 15 (2013) 19790-19798.
16. H. Zheng, G. Liu, X. Song, P. Ridgway, S. Xun, V.S. Battaglia, Cathode performance as a function of inactive material and void fractions, J. Electrochem. Soc. 157 (2010) A1060-A1066.
17. K.A. Seid, J.C. Badot, O. Dubrunfaut, S. Levasseur, D. Guyomard, B. Lestriez, Multiscale electronic transport mechanism and true conductivities in amorphous carbon-$LiFePO_4$ nanocomposites. J. Mater. Chem. 22 (2012) 2641-2649.

18. S.B. Chikkannanavar, D.M. Bernardi, L. Liu, A review of blended cathode materials for use in Li-ion batteries, J. Power Sources 248 (2014) 91-100.
19. E. Maire, J. Adrien, J.-P. Masse, E. Boller, In Situ Experiments with X ray Tomography: an Attractive Tool for Experimental Mechanics, Exp. Mech. 50 (2010) 289-305.
20. E. Maire, J.Y. Buffiere, L. Salvo, J.J. Blandin, W. Ludwig, J.M. Létang, On the application of X-ray microtomography in the field of materials science, Adv. Eng. Mater. 3 (2001) 539-546.
21. NIST X-ray attenuation Databases, http://physics.nist.gov/PhysRefData/Xcom/html/xcom1-t.html.
22. M. Schmitt, M. Baunach, L. Wengeler, K. Peters, P. Junges, P. Scharfer, W. Schabel, Slot-die processing of lithium-ion battery electrodes – coating window characterization. Chem. Eng. Process.: Process. Intensif. 68 (2013) 32-37.

Table captions

Table 1 Composition, thickness (estimated on SEM images) and porosity of NMC, LFP and blended NMC/LFP cathodes.

Table 2 Linear fitting parameters of equation (4) for Al foil, Ti foil, NMC and LFP cathodes.

Figure captions

Figure 1 Outgoing X-ray intensity histograms in electrode and air areas for (**A**) NMC and (**B**) LFP cathodes.

Figure 2 $\ln(I/I_{air})/(1-\varepsilon)$ as a function of the cathode or foil thickness, estimated on SEM images.

Figure 3 X-ray attenuation coefficients of NMC, LFP, PVdF, Cb, Al and Ti as a function of the photons energy **[21]**.

Figure 4 NMC (m-p), LFP (q-t) and blended NMC/LFP (h, d, l) cathodes thickness evaluated on SEM images and by radiography.

Figure 5 Thickness mapping of (A, B) NMC and (C, D) LFP cathodes.

Figure 6 Thickness mapping of (A) 75/25, (B) 50/50 and (C) 25/75 blended NMC/LFP cathodes.

Figure 7 Width at half maximum of the thickness histogram as a function of the average thickness for NMC, LFP and blended NMC/LFP cathodes.

Figure 8 Thickness mapping of (A) pinholes in the thickest LFP cathode (t) and (B) coating edge for the thickest NMC cathode (p)

Table 1

Ref.	NMC (vol. %)	LFP (vol. %)	PVdF (vol. %)	Cb (vol. %)	Estimated thickness (µm)	Porosity (%)
M	82.1	0	11.5	6.3	34	33
N	82.1	0	11.5	6.3	46	32
O	82.1	0	11.5	6.3	61	34
P	82.1	0	11.5	6.3	69	34
H	58.3	24.8	10.9	6.0	73	34
D	33.8	43.2	14.9	8.2	77	29
L	17.5	67.2	9.9	5.4	83	35
Q	0	85.5	9.4	5.1	44	34
R	0	85.5	9.4	5.1	61	37
S	0	85.5	9.4	5.1	76	35
T	0	85.5	9.4	5.1	88	37

Table 2

	μ (μm^{-1})	$C/(1-\varepsilon)$	R^2
NMC/Cb/PVdF	0.0027 ±0.0002	-0.041 ±0.010	0.986
LFP/Cb/PVdF	0.0016 ±0.0001	-0.021 ±0.004	0.997
Al	0.00043 ± 0.00001	-0.0005±0.0004	0.998
Ti	0.0023 ±0.0001	-0.032 ±0.007	0.993

Fig. 1

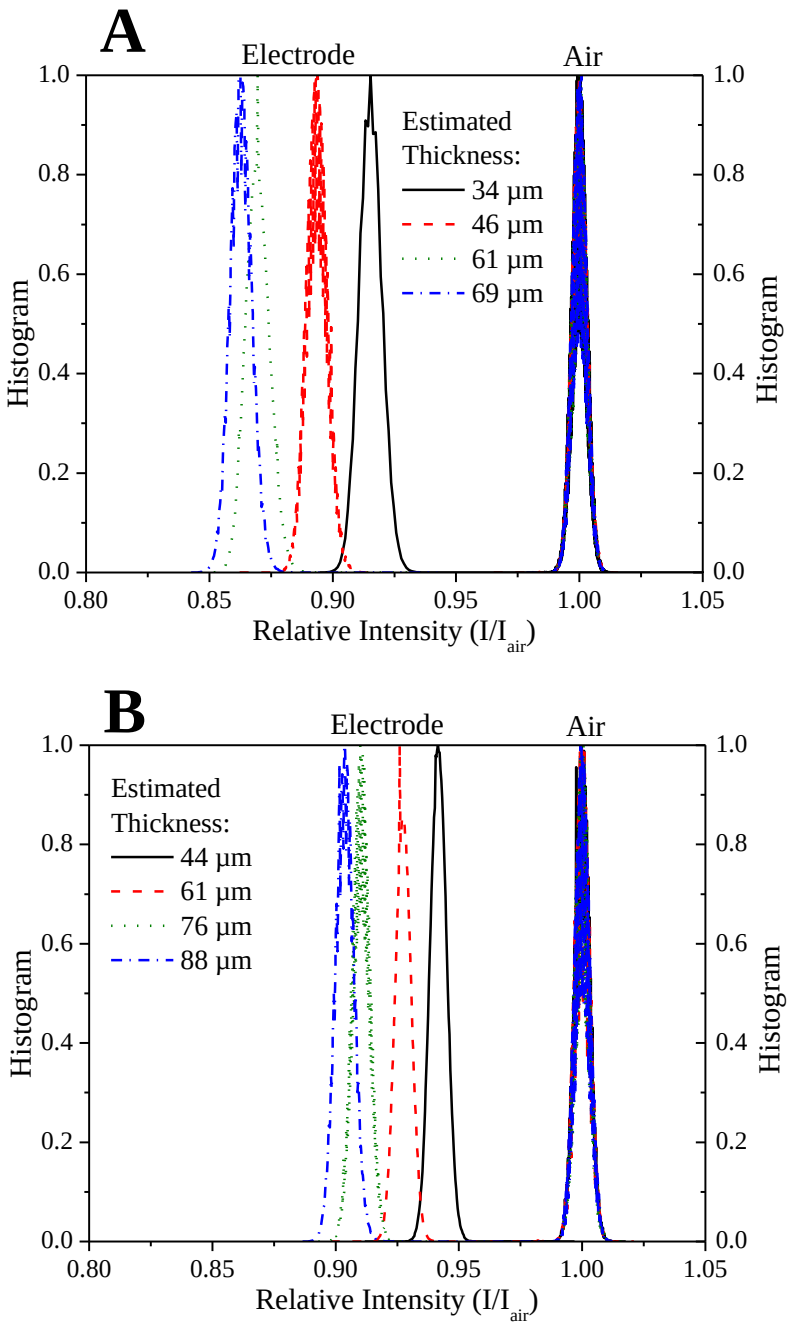
A
Electrode
Air
Estimated
Thickness:
34 µm
46 µm
61 µm
69 µm
Histogram
Relative Intensity (I/I$_{air}$)
B
Electrode
Air
Estimated
Thickness:
44 µm
61 µm
76 µm
88 µm
Histogram
Relative Intensity (I/I$_{air}$)

Fig. 2

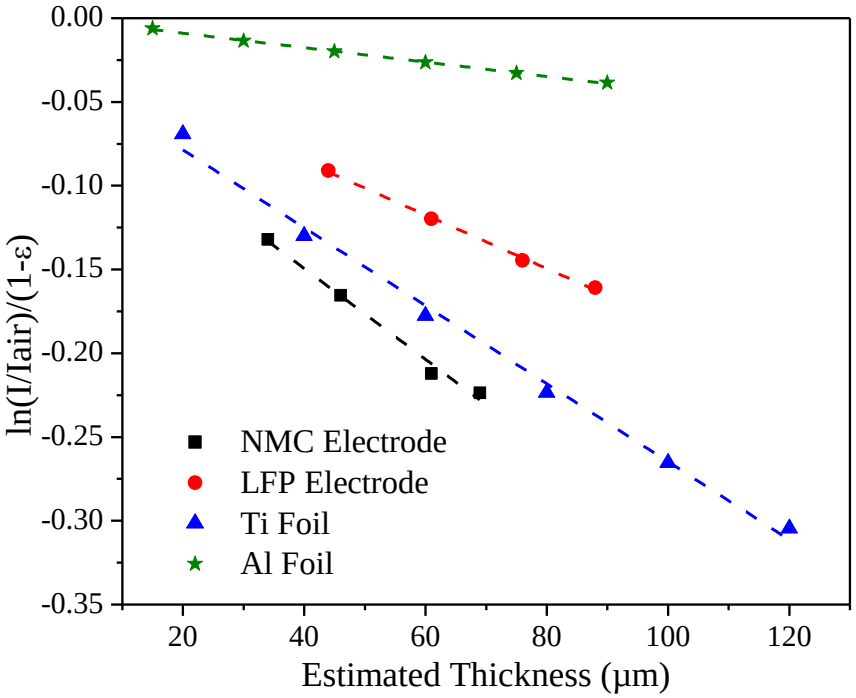
0.00
-0.05
-0.10
-0.15
-0.20
-0.25
-0.30
-0.35
ln(I/Iair)/(1-ε)
20
40
60
80
100
120
Estimated Thickness (μm)
NMC Electrode
LFP Electrode
Ti Foil
Al Foil

Fig. 3

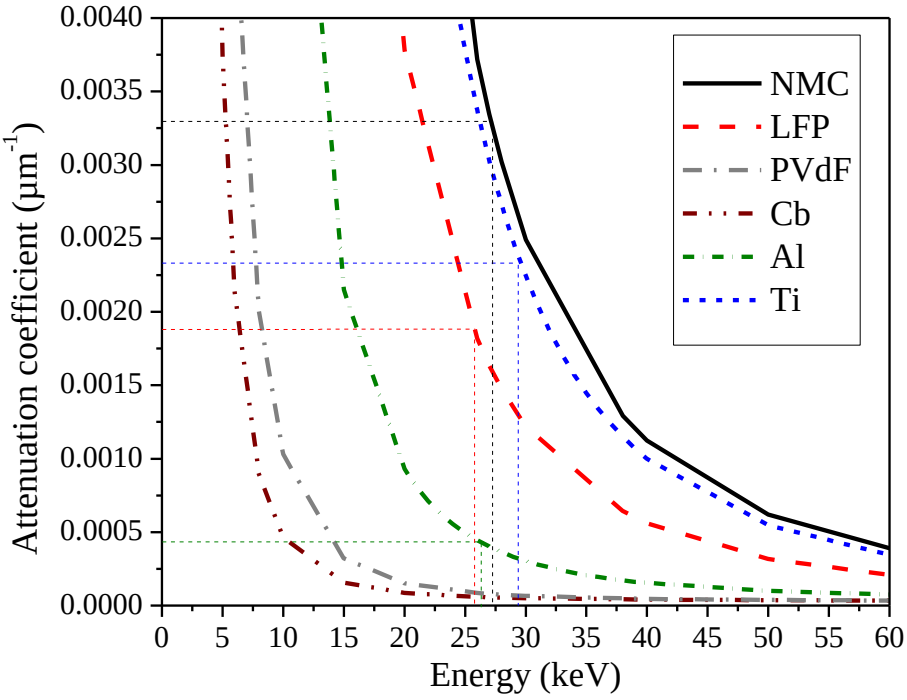
Attenuation coefficient (μm-1)
Energy (keV)
NMC
LFP
PVdF
Cb
Al
Ti
0.0040
0.0035
0.0030
0.0025
0.0020
0.0015
0.0010
0.0005
0.0000
0
5
10
15
20
25
30
35
40
45
50
55
60

Fig. 4

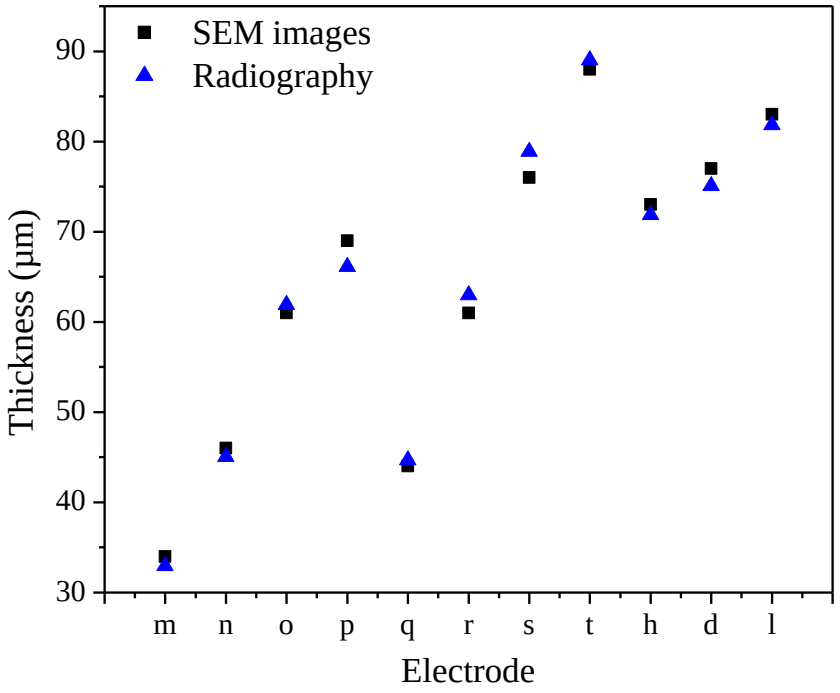
SEM images
Radiography
Thickness (µm)
90
80
70
60
50
40
30
m
n
o
p
q
r
s
t
h
d
l
Electrode

Fig. 5

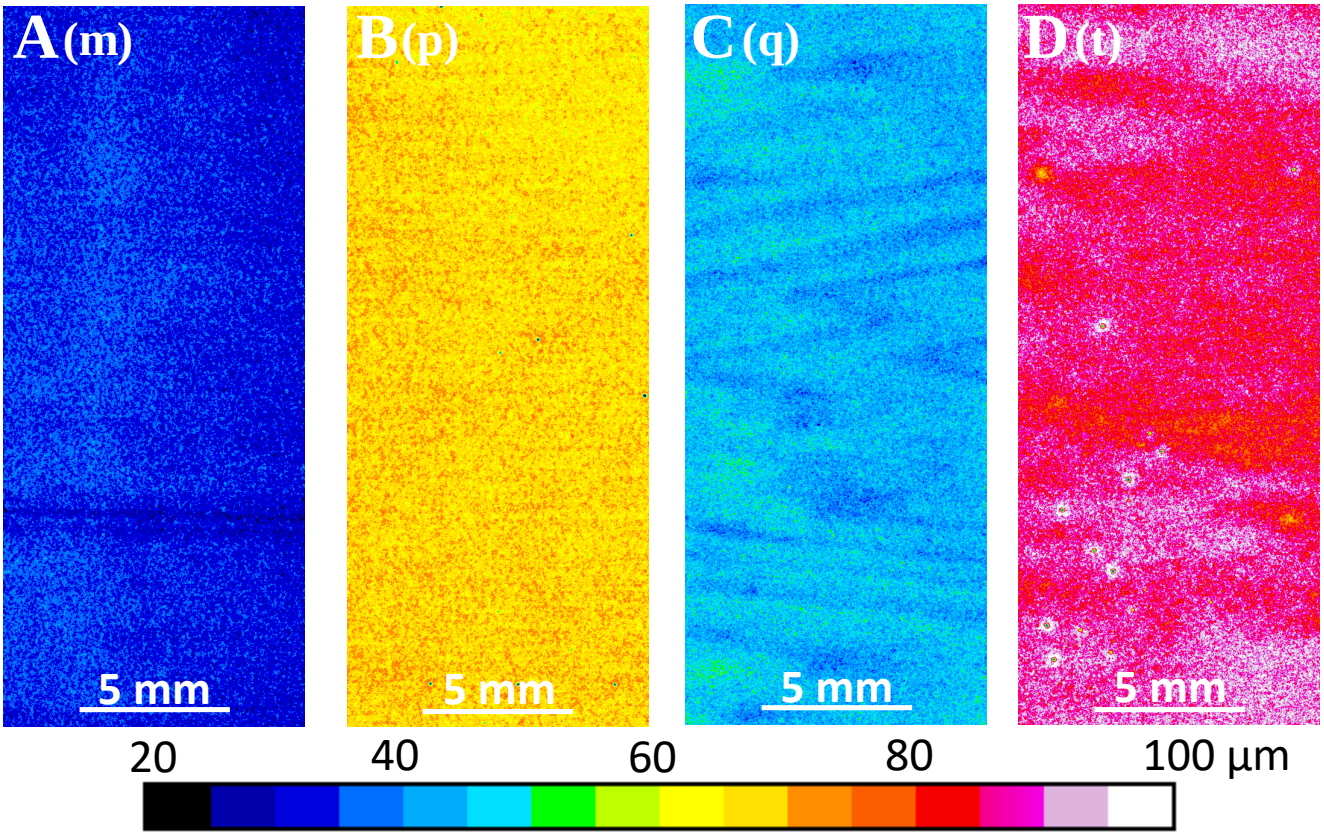

Fig. 6

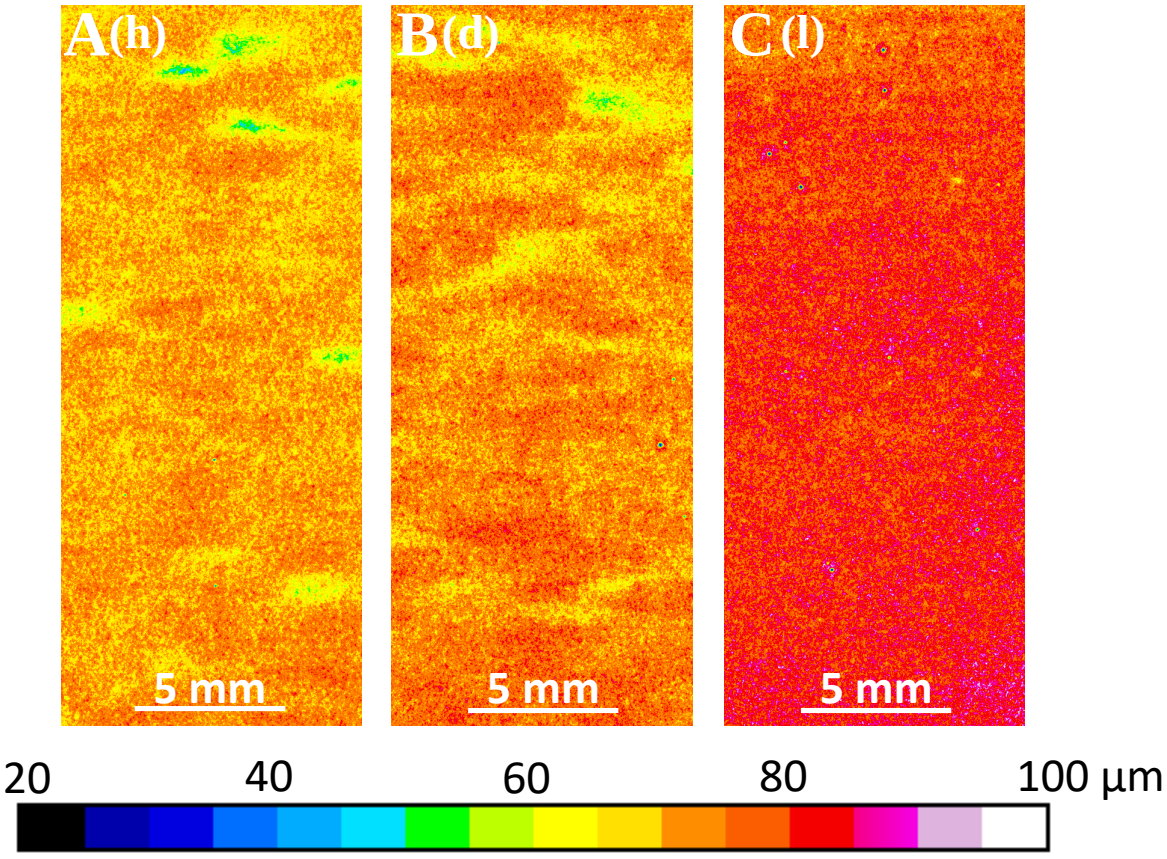

Fig. 7

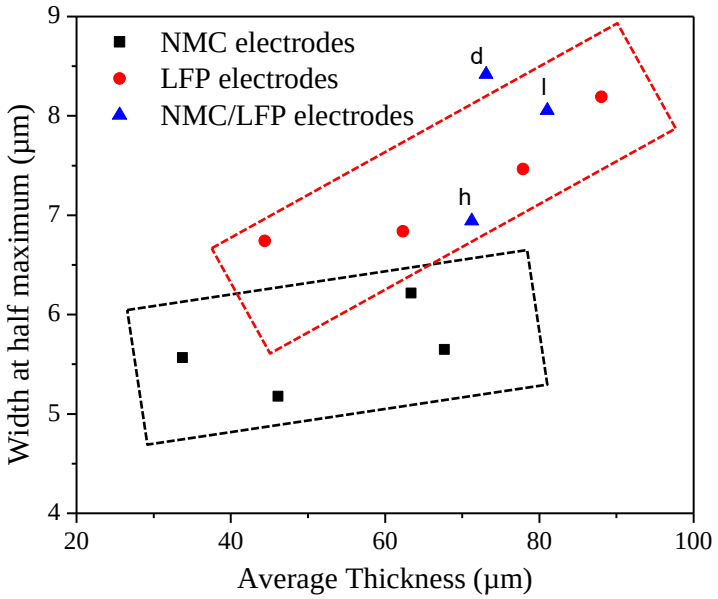
NMC electrodes
LFP electrodes
NMC/LFP electrodes
d
l
h
Width at half maximum (μm)
Average Thickness (μm)
9
8
7
6
5
4
20
40
60
80
100

Fig. 8